Mathematical and Computational Applications

MDPI

Article

A Right-Sided Cl(0,2)-Valued Linear Canonical Stockwell Transform: Rigorous Formulation and Chirp-Adaptive Computation

Yi-Qiao Xu [1,2] and Bing-Zhao Li [1,2,*]

[1] School of Mathematics and Statistics, Beijing Institute of Technology, Beijing 100081, China
[2] Beijing Key Laboratory on MCAACI, Beijing Institute of Technology, Beijing 100081, China
* Correspondence: li_bingzhao@bit.edu.cn

Abstract

Quadratic phase disperses the spectrum of chirped multicomponent data and can defeat the ordinary Stockwell analysis. We formulate a right-sided Cl(0,2)-valued linear canonical Stockwell transform (CLCST) on a positive real Hilbert space, using standard Clifford conjugation, a real scalar window, and an invariant multiplication order. Since Cl(0,2) is isomorphic to the quaternion algebra, the construction is algebraically a one-sided quaternion transform; its contribution over existing quaternion Stockwell and quaternion linear canonical Stockwell formulations is not a larger algebra but a rigorously ordered chirp–Clifford Stockwell transform (CST)–dechirp factorization, direct unit-integral-window reconstruction, and a reproducible fast Fourier transform (FFT) realization for chirp estimation. We correct the canonical output-phase ordering and specify the discrete correlation kernel and sign-preserving zero-frequency regularization. A nonsymmetric-window stress test verifies these conventions independently. The theory establishes pointwise boundedness, covariance, reconstruction, and a collapsed-energy identity. Experiments on noisy synthetic fields, a four-component signal, a Shepp–Logan phantom, and measured Hubble image content with an injected phase aberration quantify concentration, resolution, and computational cost. The results delimit rather than conceal the method's scope: it targets a global quadratic phase in Cl(0,2), while orientation sweeps, zero-mean windows, locally varying chirps, and higher-dimensional Clifford algebras require additional machinery.

Keywords: Cl(0,2); quaternion algebra; linear canonical transform; Stockwell transform; chirp estimation; fast Fourier transform algorithm; multicomponent signal

MSC: 42B10; 42C40; 65T50; 94A12

Check for updates

Academic Editor: Gianluigi Rozza

Received: 13 August 2026
Revised: 19 September 2026
Accepted: 23 September 2026
Published: 24 September 2026

Copyright: © 2026 by the authors. Licensee MDPI, Basel, Switzerland. This article is an open access article distributed under the terms and conditions of the Creative Commons Attribution (CC BY) license.

1. Introduction

The Stockwell transform (ST) combines a frequency-dependent analyzing window with a Fourier carrier and has been used to localize nonstationary spectral content [1–3]. Continuous and multidimensional formulations clarify its inversion and localization structure [4,5]. In parallel, the linear canonical transform (LCT) and its fractional Fourier special case provide a natural coordinate system for quadratic-phase signals [6,7]. The fractional Stockwell transform (FrST) and linear canonical Stockwell transform (LCST) exploit this fact for complex-valued chirps [8,9]. Clifford- and quaternion-valued Stockwell transforms encode multicomponent signals in a single algebra-valued field [10,11], while a two-sided quaternion linear canonical S-transform (Q-LCST) has already been studied

theoretically [12]. Efficient quaternion Fourier implementations based on two complex fast Fourier transforms (FFTs) are also established [13]. These results make comparison with quaternion formulations essential rather than optional.

A formal replacement of the Fourier kernel by a canonical kernel, however, is not sufficient. Three issues are decisive. First, the involution used in the signal space must make the L^2 norm positive, and a real Hilbert inner product must not be identified with a Clifford-valued pairing. Second, the side and order of all phase factors must be fixed because Clifford multiplication is noncommutative. Third, a proposed transform should identify a phenomenon unavailable to the ordinary Clifford Stockwell transform (CST), and that phenomenon should be supported by a fully specified algorithm and quantitative comparisons rather than parameter plots alone.

This article addresses those issues by deliberately restricting the algebraic setting to $\mathrm{Cl}_{0,2}$. Because $\mathrm{Cl}_{0,2} \cong \mathbb{H}$, the four real coefficient channels and the multiplicative coefficient norm are exactly quaternionic; consequently, we do not claim a broader algebraic generalization or an intrinsic speed or accuracy advantage over a one-sided quaternion implementation. The precise added value is instead the right-sided convention, the exact chirp-conjugation identity, the direct reconstruction route, and their matched, sign-consistent FFT algorithm. The pseudoscalar $I = e_1e_2$ satisfies $I^2 = -1$, so it generates a fixed complex subalgebra for all right-sided oscillatory factors. Signals remain fully $\mathrm{Cl}_{0,2}$-valued, but the window is real and scalar. This scope avoids dimension-dependent assertions about the pseudoscalar in a general $\mathrm{Cl}_{0,n}$ and makes the implemented transform identical to the analyzed one.

The contributions are as follows:

(i) We define the right-sided Cl(0,2)-valued linear canonical Stockwell transform (CLCST) on a positive real Hilbert space and distinguish it from the associated Clifford-valued pairing. We also show exactly how a canonical matrix $M = (A, B; C, D)$ reduces to the chirp ratio $\gamma = A/(2B)$ after output rescaling and dephasing.

(ii) We prove an exact factorization into chirp multiplication, the CST, and output dechirping. This yields the central mechanism: a quadratic-phase component $a(x)e^{-I\kappa\|x\|^2}$ becomes the unchirped envelope when $\gamma = \kappa$.

(iii) We establish boundedness, covariance, direct reconstruction, and a collapsed-energy identity. No full coefficient-space Parseval formula, admissibility constant, or reproducing-kernel claim is made, because those statements require a separate window-dependent frame analysis.

(iv) We provide an FFT-assisted discrete algorithm with an explicit reversed convolution kernel and a sign-preserving convention at zero frequency. A nonsymmetric-window stress test exposes errors that a symmetric Gaussian would mask. Quantitative CST comparisons then assess concentration, resolution, noise, four-component behavior, a Shepp–Logan benchmark, and measured Hubble image content.

The rest of the article is organized as follows. Section 2 fixes the algebra and Fourier conventions. Section 3 defines the transform and proves its properties. Section 4 gives the discrete algorithm and concentration measures. Section 5 reports the numerical results, Section 6 discusses interpretation and limitations, and the final section gives the conclusions.

2. Algebraic and Analytic Setting

2.1. The Algebra $Cl_{0,2}$ and a Positive Signal Space

The real Clifford algebra $\mathrm{Cl}_{0,2}$ is generated by e_1, e_2 with

$$e_1^2 = e_2^2 = -1, \qquad e_1e_2 = -e_2e_1. \tag{1}$$

Writing $I = e_1e_2$, every $a \in \mathrm{Cl}_{0,2}$ has the unique expansion

$$a = a_0 + a_1e_1 + a_2e_2 + a_{12}I, \qquad I^2 = -1. \tag{2}$$

Standard Clifford conjugation is denoted by an overbar [14]:

$$\overline{a} = a_0 - a_1e_1 - a_2e_2 - a_{12}I, \tag{3}$$

and the coefficient norm is

$$|a|_c^2 = \mathrm{Sc}(a\overline{a}) = a_0^2 + a_1^2 + a_2^2 + a_{12}^2. \tag{4}$$

This is the quaternion norm, hence $|ab|_c = |a|_c|b|_c$. In particular, $\left|e^{It}\right|_c = 1$ for $e^{It} = \cos t + I \sin t$.

Explicitly, $1 \mapsto 1$, $e_1 \mapsto \boldsymbol{i}$, $e_2 \mapsto \boldsymbol{j}$, and $I = e_1e_2 \mapsto \boldsymbol{k}$ define an algebra isomorphism $\mathrm{Cl}_{0,2} \to \mathbb{H}$. The Clifford notation is useful here because it ties the chosen pseudoscalar and spatial basis to the CFT convention, but it does not enlarge the quaternionic signal class.

For measurable $f, g : \mathbb{R}^2 \to \mathrm{Cl}_{0,2}$, the real Hilbert inner product and norm are

$$(f,g)_{\mathbb{R}} = \int_{\mathbb{R}^2} \mathrm{Sc}\Big(f(x)\overline{g(x)}\Big)\,dx, \qquad \|f\|_2^2 = \int_{\mathbb{R}^2} |f(x)|_c^2\,dx. \tag{5}$$

The Clifford-valued pairing

$$[f,g]_{\mathrm{Cl}_{0,2}} = \int_{\mathbb{R}^2} f(x)\overline{g(x)}\,dx \tag{6}$$

is useful algebraically, but it is not the real Hilbert inner product in (5). All norm and energy statements below refer to the real scalar structure.

2.2. Right-Sided Clifford Fourier and Stockwell Transforms

Following the right-sided Clifford Fourier transform (CFT) convention in [10,15], for $h \in L^1(\mathbb{R}^2, \mathrm{Cl}_{0,2}) \cap L^2(\mathbb{R}^2, \mathrm{Cl}_{0,2})$, define

$$(\mathcal{F}_R h)(u) = \widehat{h}(u) = \frac{1}{2\pi} \int_{\mathbb{R}^2} h(x) e^{-Ix\cdot u}\,dx, \tag{7}$$

with inverse

$$h(x) = \frac{1}{2\pi} \int_{\mathbb{R}^2} \widehat{h}(u) e^{Ix\cdot u}\,du. \tag{8}$$

The symmetric two-dimensional normalization makes $\mathcal{F}_R$ unitary in the coefficient norm:

$$\int_{\mathbb{R}^2} \left|\widehat{h}(u)\right|_c^2 du = \int_{\mathbb{R}^2} |h(x)|_c^2\,dx. \tag{9}$$

Let $\psi \in L^1(\mathbb{R}^2) \cap L^2(\mathbb{R}^2)$ be real-valued. For $u = (u_1, u_2) \in \mathcal{U} = (\mathbb{R} \setminus \{0\})^2$, set

$$D_u = \mathrm{diag}(u_1, u_2), \qquad R_\theta = \begin{pmatrix} \cos\theta & -\sin\theta \\ \sin\theta & \cos\theta \end{pmatrix}, \tag{10}$$

and define

$$w_{b,u,\theta}(x) = |\det D_u|\, \psi(R_{-\theta} D_u (x - b)). \tag{11}$$

If $\int \psi = 1$, then $\int_{\mathbb{R}^2} w_{b,u,\theta}(x)\,db = 1$ for every fixed x, u, θ. The corresponding right-sided CST [10] is

$$(\mathcal{S}_\psi^R f)(b,u,\theta) = \frac{1}{2\pi} \int_{\mathbb{R}^2} f(x) w_{b,u,\theta}(x) e^{-Ix\cdot u}\,dx. \tag{12}$$

The real scalar window is important: it commutes with every Clifford value and introduces no hidden factor reordering.

3. Right-Sided Clifford Linear Canonical Stockwell Transform

3.1. Definition and Precise Canonical Dependence

For $\gamma \in \mathbb{R}$, introduce the unitary right-chirp operator

$$(C_\gamma f)(x) = f(x)e^{I\gamma\|x\|^2}. \tag{13}$$

Definition 1 (Right-sided CLCST). *Let $f \in L^2(\mathbb{R}^2, \mathrm{Cl}_{0,2})$ and let ψ be a real scalar window. The right-sided Clifford linear canonical Stockwell transform with chirp ratio γ is*

$$(\mathcal{S}^R_{\psi,\gamma} f)(b,u,\theta) = \frac{1}{2\pi}\int_{\mathbb{R}^2} f(x)e^{I\gamma\|x\|^2} w_{b,u,\theta}(x)e^{-Ix\cdot u}\,dx\,e^{-I\gamma\|b\|^2}, \tag{14}$$

where $b \in \mathbb{R}^2$, $u \in \mathcal{U}$, and $\theta \in [0, 2\pi)$. All exponential factors act on the right in the displayed order.

The terminology "linear canonical" comes from the following exact relation. For a scalar symplectic matrix

$$M = \begin{pmatrix} A & B \\ C & D \end{pmatrix}, \qquad AD - BC = 1, \qquad B \neq 0, \tag{15}$$

use the explicit right Clifford linear canonical transform (CLCT) convention [16]

$$(\mathcal{L}^R_M g)(\omega) = \frac{1}{2\pi|B|}\int_{\mathbb{R}^2} g(x)\exp\left[\frac{I}{2B}\left(A\|x\|^2 - 2x\cdot\omega + D\|\omega\|^2\right)\right]dx. \tag{16}$$

Other kernel conventions can differ from (16) by a constant unit-modulus branch factor. Put $\gamma = A/(2B)$ and $g_{b,u,\theta}(x) = f(x)w_{b,u,\theta}(x)$. Evaluating (16) at $\omega = Bu$ gives

$$\begin{aligned}(\mathcal{L}^R_M g_{b,u,\theta})(Bu) &= \frac{1}{2\pi|B|}\int_{\mathbb{R}^2} f(x)w_{b,u,\theta}(x)\exp\left[\frac{I}{2B}\left(A\|x\|^2 - 2Bx\cdot u + DB^2\|u\|^2\right)\right]dx \\ &= \frac{1}{2\pi|B|}\left[\int_{\mathbb{R}^2} f(x)e^{I\gamma\|x\|^2}w_{b,u,\theta}(x)e^{-Ix\cdot u}\,dx\right]e^{I(DB/2)\|u\|^2}.\end{aligned}$$

Here, the three exponentials belong to the same commutative subalgebra $\mathrm{span}\{1, I\}$, so they may be separated without changing their order relative to $f(x)$. The x-independent phase must nevertheless remain on the right of the Clifford-valued integral. The scalar window may be moved across a phase, whereas no Clifford-valued phase is moved through the signal or the integral. Right-multiplying by the inverse output phase therefore gives

$$\begin{aligned}&|B|(\mathcal{L}^R_M g_{b,u,\theta})(Bu)e^{-I(DB/2)\|u\|^2}e^{-I\gamma\|b\|^2} \\ &\quad= \frac{1}{2\pi}\int_{\mathbb{R}^2} f(x)e^{I\gamma\|x\|^2}w_{b,u,\theta}(x)e^{-Ix\cdot u}\,dx\,e^{-I\gamma\|b\|^2} \\ &\quad= (\mathcal{S}^R_{\psi,\gamma} f)(b,u,\theta).\end{aligned}$$

Equivalently,

$$(\mathcal{S}^R_{\psi,\gamma} f)(b,u,\theta) = |B|\,(\mathcal{L}^R_M g_{b,u,\theta})(Bu)e^{-I(DB/2)\|u\|^2}e^{-I\gamma\|b\|^2}. \tag{17}$$

Thus, after frequency rescaling and right-sided removal of a known output phase, the analysis depends on M only through $A/B = 2\gamma$. The construction is not claimed to be a

genuinely independent four-parameter transform. Equation (17) also removes any ambiguity concerning the normalization used in two dimensions and makes the noncommutative multiplication order explicit.

Figure 1 summarizes the canonical-domain construction and the required order of its output operations.

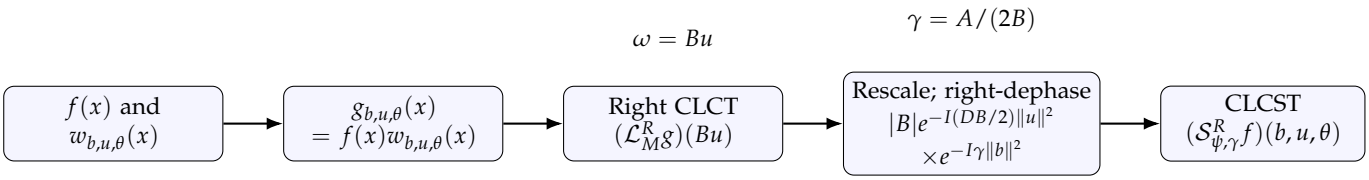

Figure 1. Canonical-domain construction of the right-sided Clifford linear canonical Stockwell transform (CLCST). The Clifford linear canonical transform (CLCT) is evaluated at the rescaled frequency and followed by known output operations.

3.2. Factorization and the Chirp-Matching Mechanism

Proposition 1 (Exact factorization)**.** *For every admissible parameter tuple,*

$$(\mathcal{S}_{\psi,\gamma}^R f)(b,u,\theta) = (\mathcal{S}_{\psi}^R C_\gamma f)(b,u,\theta)e^{-I\gamma\|b\|^2}. \tag{18}$$

In particular, $\mathcal{S}_{\psi,0}^R = \mathcal{S}_{\psi}^R$.

Proof. By (13) and (12),

$$\begin{aligned}(\mathcal{S}_{\psi}^R C_\gamma f)(b,u,\theta) &= \frac{1}{2\pi}\int_{\mathbb{R}^2}(C_\gamma f)(x)w_{b,u,\theta}(x)e^{-Ix\cdot u}\,dx \\ &= \frac{1}{2\pi}\int_{\mathbb{R}^2} f(x)e^{I\gamma\|x\|^2}w_{b,u,\theta}(x)e^{-Ix\cdot u}\,dx.\end{aligned}$$

The window is real, so this is the same ordered integrand as in (14). Therefore,

$$\begin{aligned}(\mathcal{S}_{\psi}^R C_\gamma f)(b,u,\theta)e^{-I\gamma\|b\|^2} &= \frac{1}{2\pi}\int_{\mathbb{R}^2} f(x)e^{I\gamma\|x\|^2}w_{b,u,\theta}(x)e^{-Ix\cdot u}\,dx\,e^{-I\gamma\|b\|^2} \\ &= (\mathcal{S}_{\psi,\gamma}^R f)(b,u,\theta).\end{aligned}$$

Setting $\gamma = 0$ makes both chirp factors equal to one and gives $\mathcal{S}_{\psi,0}^R = \mathcal{S}_{\psi}^R$. □

Equation (18) is an operator identity, not only a visual similarity between analyzing functions. It also identifies what becomes possible when γ is varied.

Figure 2 displays the corresponding chirp–CST–dechirp computational flow.

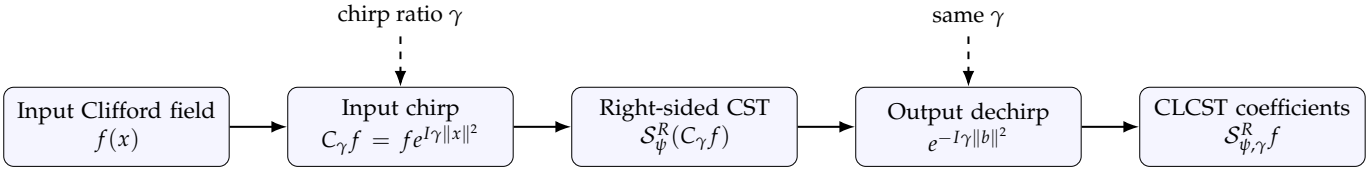

Figure 2. Factorized computational flow of the CLCST. The middle block is the ordinary Clifford Stockwell transform (CST); the two chirp multiplications supply the canonical phase adaptation.

Corollary 1 (Matched dechirping)**.** *Let*

$$f_\kappa(x) = a(x)e^{-I\kappa\|x\|^2}, \qquad a \in L^2(\mathbb{R}^2, \mathrm{Cl}_{0,2}). \tag{19}$$

At $\gamma = \kappa$,

$$(\mathcal{S}_{\psi,\kappa}^R f_\kappa)(b,u,\theta) = (\mathcal{S}_{\psi}^R a)(b,u,\theta)e^{-I\kappa\|b\|^2}, \tag{20}$$

and therefore

$$\left|(\mathcal{S}^R_{\psi,\kappa} f_\kappa)(b,u,\theta)\right|_c = \left|(\mathcal{S}^R_{\psi} a)(b,u,\theta)\right|_c. \tag{21}$$

The CST corresponds to the single value $\gamma = 0$ and cannot perform the parameter scan in (20). This is the specific additional mechanism assessed quantitatively in Section 5.

3.3. Boundedness and Covariance

Proposition 2 (Pointwise bound). *For $f \in L^2(\mathbb{R}^2, \mathrm{Cl}_{0,2})$ and $\psi \in L^2(\mathbb{R}^2)$,*

$$\left|(\mathcal{S}^R_{\psi,\gamma} f)(b,u,\theta)\right|_c \le \frac{|\det D_u|^{1/2}}{2\pi} \|f\|_2 \|\psi\|_2. \tag{22}$$

Proof. Both chirp factors have coefficient norm one. First, with $y = R_{-\theta} D_u (x-b)$ and $dx = |\det D_u|^{-1} dy$,

$$\begin{aligned} \|w_{b,u,\theta}\|_2^2 &= |\det D_u|^2 \int_{\mathbb{R}^2} |\psi(R_{-\theta} D_u (x-b))|^2 dx \\ &= |\det D_u|^2 |\det D_u|^{-1} \int_{\mathbb{R}^2} |\psi(y)|^2 dy \\ &= |\det D_u| \, \|\psi\|_2^2. \end{aligned}$$

Using the multiplicativity of the coefficient norm and then Cauchy–Schwarz gives

$$\begin{aligned} \left|(\mathcal{S}^R_{\psi,\gamma} f)(b,u,\theta)\right|_c &\le \frac{1}{2\pi} \int_{\mathbb{R}^2} |f(x)|_c \, |w_{b,u,\theta}(x)| \, dx \\ &\le \frac{1}{2\pi} \|f\|_2 \|w_{b,u,\theta}\|_2 \\ &= \frac{|\det D_u|^{1/2}}{2\pi} \|f\|_2 \|\psi\|_2, \end{aligned}$$

which is (22). □

Let $(T_k f)(x) = f(x-k)$ and $(M^R_v f)(x) = f(x) e^{Ix\cdot v}$. Translation does not merely shift the frequency index because the Stockwell window itself depends on u.

Proposition 3 (Translation covariance). *For $k \in \mathbb{R}^2$,*

$$\begin{aligned} (\mathcal{S}^R_{\psi,\gamma} T_k f)(b,u,\theta) = (\mathcal{S}^R_{\psi,\gamma} M^R_{2\gamma k} f)(b-k,u,\theta) \\ \times e^{I\{2\gamma(\|k\|^2 - b\cdot k) - k\cdot u\}}. \end{aligned} \tag{23}$$

For $\gamma = 0$, this reduces to the standard CST rule $(\mathcal{S}^R_{\psi} T_k f)(b,u,\theta) = (\mathcal{S}^R_{\psi} f)(b-k,u,\theta) e^{-Ik\cdot u}$.

Proof. Put $x = y + k$ in (14). Since

$$w_{b,u,\theta}(y+k) = w_{b-k,u,\theta}(y), \qquad \|y+k\|^2 = \|y\|^2 + 2y\cdot k + \|k\|^2,$$

we obtain

$$\begin{aligned} (\mathcal{S}^R_{\psi,\gamma} T_k f)(b,u,\theta) = \frac{1}{2\pi} \int_{\mathbb{R}^2} f(y) e^{I\gamma\|y\|^2} e^{I2\gamma y\cdot k} w_{b-k,u,\theta}(y) e^{-Iy\cdot u} \, dy \\ \times e^{I\{\gamma\|k\|^2 - k\cdot u - \gamma\|b\|^2\}}. \end{aligned}$$

On the other hand, the definition of $M^R_{2\gamma k}$ gives

$$(\mathcal{S}^R_{\psi,\gamma} M^R_{2\gamma k} f)(b-k,u,\theta) = \frac{1}{2\pi}\int_{\mathbb{R}^2} f(y) e^{I2\gamma y\cdot k} e^{I\gamma\|y\|^2} w_{b-k,u,\theta}(y) e^{-Iy\cdot u}\, dy \times e^{-I\gamma\|b-k\|^2}.$$

All exponential factors belong to $\mathrm{span}\{1, I\}$, so the two chirp factors commute with each other while remaining to the right of $f(y)$. Their external phase ratio is

$$\begin{aligned}&\gamma\|b-k\|^2 + \gamma\|k\|^2 - k\cdot u - \gamma\|b\|^2\\ &\quad = 2\gamma(\|k\|^2 - b\cdot k) - k\cdot u.\end{aligned}$$

Substitution of this identity proves (23); setting $\gamma = 0$ gives the stated CST rule. □

Proposition 4 (Positive dilation and parity)**.** *For $\lambda > 0$, let $(D_\lambda f)(x) = f(\lambda x)$, and let $(Pf)(x) = f(-x)$. Then*

$$(\mathcal{S}^R_{\psi,\gamma} D_\lambda f)(b,u,\theta) = (\mathcal{S}^R_{\psi,\gamma/\lambda^2} f)(\lambda b, u/\lambda, \theta), \tag{24}$$

$$(\mathcal{S}^R_{\psi,\gamma} Pf)(b,u,\theta) = (\mathcal{S}^R_{\psi,\gamma} f)(-b,-u,\theta). \tag{25}$$

Proof. For the dilation, put $y = \lambda x$, so $dx = \lambda^{-2} dy$. The window and phase terms become

$$\begin{aligned}\lambda^{-2}|\det D_u| &= |\det D_{u/\lambda}|,\\ R_{-\theta} D_u (x-b) &= R_{-\theta} D_{u/\lambda}(y - \lambda b),\\ \gamma\|x\|^2 &= (\gamma/\lambda^2)\|y\|^2,\\ x\cdot u &= y\cdot(u/\lambda),\\ \gamma\|b\|^2 &= (\gamma/\lambda^2)\|\lambda b\|^2.\end{aligned}$$

Consequently,

$$\begin{aligned}(\mathcal{S}^R_{\psi,\gamma} D_\lambda f)(b,u,\theta) &= \frac{1}{2\pi}\int_{\mathbb{R}^2} f(y) e^{I(\gamma/\lambda^2)\|y\|^2} w_{\lambda b, u/\lambda,\theta}(y) e^{-Iy\cdot(u/\lambda)}\, dy\\ &\quad \times e^{-I(\gamma/\lambda^2)\|\lambda b\|^2}\\ &= (\mathcal{S}^R_{\psi,\gamma/\lambda^2} f)(\lambda b, u/\lambda, \theta),\end{aligned}$$

which proves (24).

For parity, put $y = -x$. Since $D_{-u} = -D_u$,

$$w_{b,u,\theta}(-y) = |\det D_{-u}|\psi(R_{-\theta} D_{-u}(y+b)) = w_{-b,-u,\theta}(y).$$

It follows that

$$\begin{aligned}(\mathcal{S}^R_{\psi,\gamma} Pf)(b,u,\theta) &= \frac{1}{2\pi}\int_{\mathbb{R}^2} f(y) e^{I\gamma\|y\|^2} w_{-b,-u,\theta}(y) e^{-Iy\cdot(-u)}\, dy\, e^{-I\gamma\|-b\|^2}\\ &= (\mathcal{S}^R_{\psi,\gamma} f)(-b,-u,\theta),\end{aligned}$$

which is (25). No dimension-dependent sign is introduced. □

3.4. Direct Inversion and Collapsed Energy

The reconstruction window must have nonzero integral. This requirement separates the Gaussian window used below from zero-mean derivative-of-Gaussian (DOG) windows:

a DOG window may be useful for feature localization, but it cannot be inserted into the following inversion formula.

Theorem 1 (Collapse identity and inversion)**.** *Assume $\psi \in L^1(\mathbb{R}^2) \cap L^2(\mathbb{R}^2)$ is real and*

$$\int_{\mathbb{R}^2} \psi(y)\, dy = 1. \tag{26}$$

For f in the Schwartz class, and hence by density in the corresponding L^2 sense, define

$$G_\gamma f(u) = \int_{\mathbb{R}^2} (\mathcal{S}^R_{\psi,\gamma} f)(b,u,\theta) e^{I\gamma\|b\|^2}\, db. \tag{27}$$

Then $G_\gamma f$ is independent of θ and

$$G_\gamma f = \mathcal{F}_R(C_\gamma f). \tag{28}$$

Consequently,

$$f(x) = \mathcal{F}_R^{-1}(G_\gamma f)(x) e^{-I\gamma\|x\|^2}, \tag{29}$$

and the exact scalar energy identity

$$\int_{\mathbb{R}^2} |G_\gamma f(u)|_c^2\, du = \|f\|_2^2 \tag{30}$$

holds.

Proof. For fixed x, u, θ, set

$$y = R_{-\theta} D_u (x - b), \qquad b = x - D_u^{-1} R_\theta y, \qquad db = |\det D_u|^{-1} dy.$$

The window normalization then gives

$$\begin{aligned} \int_{\mathbb{R}^2} w_{b,u,\theta}(x)\, db &= |\det D_u| \int_{\mathbb{R}^2} \psi(R_{-\theta} D_u (x-b)) db \\ &= |\det D_u|\, |\det D_u|^{-1} \int_{\mathbb{R}^2} \psi(y)\, dy = 1. \end{aligned} \tag{31}$$

For Schwartz-class f, the integrands are absolutely integrable, so Fubini's theorem permits the order of integration to be exchanged. Substitution of (14) into (27) gives

$$\begin{aligned} G_\gamma f(u) &= \int_{\mathbb{R}^2} \left[\frac{1}{2\pi} \int_{\mathbb{R}^2} f(x) e^{I\gamma\|x\|^2} w_{b,u,\theta}(x) e^{-Ix\cdot u}\, dx\, e^{-I\gamma\|b\|^2} \right] e^{I\gamma\|b\|^2}\, db \\ &= \frac{1}{2\pi} \int_{\mathbb{R}^2} f(x) e^{I\gamma\|x\|^2} e^{-Ix\cdot u} \left[\int_{\mathbb{R}^2} w_{b,u,\theta}(x)\, db \right] dx \\ &= \frac{1}{2\pi} \int_{\mathbb{R}^2} f(x) e^{I\gamma\|x\|^2} e^{-Ix\cdot u}\, dx \\ &= (\mathcal{F}_R C_\gamma f)(u). \end{aligned} \tag{32}$$

This expression contains no θ, which proves both the claimed independence and (28). Applying the inverse CFT yields

$$\begin{aligned} \mathcal{F}_R^{-1}(G_\gamma f)(x) = (C_\gamma f)(x) = f(x) e^{I\gamma\|x\|^2}, \\ \mathcal{F}_R^{-1}(G_\gamma f)(x) e^{-I\gamma\|x\|^2} = f(x), \end{aligned}$$

which is (29). Finally, Plancherel's identity and $\left|e^{I\gamma\|x\|^2}\right|_c = 1$ give

$$\int_{\mathbb{R}^2} |G_\gamma f(u)|_c^2 \, du = \|\mathcal{F}_R(C_\gamma f)\|_2^2 = \|C_\gamma f\|_2^2 = \int_{\mathbb{R}^2} \left| f(x) e^{I\gamma\|x\|^2} \right|_c^2 dx = \|f\|_2^2.$$

The identities extend from the Schwartz class by density and continuity in the stated L^2 sense. □

The coordinate axes omitted from $\mathcal{U}$ have Lebesgue measure zero and do not affect the L^2 inverse Fourier integral. Theorem 1 is not a Parseval identity over the full (b, u, θ) coefficient space. Establishing such a continuous-frame identity would require a window-dependent measure and admissibility analysis and lies outside the present claims.

4. FFT-Assisted Discretization and Quantitative Measures

4.1. Two-Complex-Array Representation of $Cl_{0,2}$

The implementation stores

$$f = f_0 + f_1 e_1 + f_2 e_2 + f_{12} I \tag{33}$$

as two complex arrays

$$z_0 = f_0 + \mathrm{i} f_{12}, \qquad z_1 = f_1 - \mathrm{i} f_2. \tag{34}$$

Right multiplication by e^{It} is ordinary complex multiplication of both arrays by $e^{\mathrm{i}t}$, and

$$|f|_c^2 = |z_0|^2 + |z_1|^2. \tag{35}$$

Thus, the code evaluates the complete $\mathrm{Cl}_{0,2}$ transform rather than four unrelated scalar plots, while using standard complex FFT routines. This representation is the usual quaternion split-complex idea [13]; it does not by itself make the proposed method faster than an equivalent one-sided quaternion algorithm.

For comparison, left multiplication by e^{It} maps the same pair to $(e^{\mathrm{i}t} z_0, e^{-\mathrm{i}t} z_1)$. Hence a consistently rederived left-sided transform can also be implemented by two complex arrays and has the same leading complexity, but its second array uses the opposite Fourier sign and its phase-order identities are not interchangeable with the right-sided formulas proved here.

4.2. Discrete Algorithm, Zero Frequency, and Complexity

Let a rectangular periodic grid contain $N = N_1 N_2$ samples with cell area $\Delta x = \Delta x_1 \Delta x_2$. For a sampled frequency u, let u^* denote the sign-preserving regularized scale defined below and sample the centered offset kernel

$$\kappa_{u,\theta}[r] = |\det D_{u^*}| \, \psi(R_{-\theta} D_{u^*} x_r), \qquad \kappa_{u,\theta}^{\vee}[r] = \kappa_{u,\theta}[-r \pmod{(N_1, N_2)}]. \tag{36}$$

The samples are normalized so that $\Delta x \sum_r \kappa_{u,\theta}[r] = 1$. Since $w_{b_m,u,\theta}(x_n) = \kappa_{u,\theta}[n - m]$, the defining discrete coefficient is

$$S_u[m] = \frac{\Delta x}{2\pi} \sum_n q_u[n] \kappa_{u,\theta}[n - m] e^{-I\gamma\|b_m\|^2}, \qquad q_u[n] = f[n] e^{I\gamma\|x_n\|^2} e^{-I x_n \cdot u}. \tag{37}$$

Thus S_u is a circular correlation of q_u with $\kappa_{u,\theta}$, or equivalently a circular convolution with the reversed kernel $\kappa_{u,\theta}^{\vee}$. For each u, the following steps compute all translations b_m:

Step 1: Chirp the signal once: $h[n] = f[n]e^{I\gamma\|x_n\|^2}$.
Step 2: Modulate it: $q_u[n] = h[n]e^{-Ix_n\cdot u}$.
Step 3: Sample and periodically center $\kappa_{u,\theta}[r]$, renormalize it, and form $\kappa^{\vee}_{u,\theta}[r] = \kappa_{u,\theta}[-r]$.
Step 4: Compute the circular convolution for all b_m,

$$S_u[m] = \frac{\Delta x}{2\pi}\,\mathrm{IFFT}\big\{\mathrm{FFT}(q_u)\,\mathrm{FFT}(\kappa^{\vee}_{u,\theta})\big\}[m]e^{-I\gamma\|b_m\|^2}. \tag{38}$$

The continuous definition excludes $u_1u_2 = 0$. A discrete Fourier grid necessarily contains zero. In the window only, the implementation uses the sign-preserving scale floor

$$u_j^* = \mathrm{sgn}_0(u_j)\max\{|u_j|, 2\pi/L_j\}, \qquad \mathrm{sgn}_0(t) = \begin{cases} 1, & t \geq 0, \\ -1, & t < 0, \end{cases} \tag{39}$$

where $L_j = N_j\Delta x_j$; the carrier retains its actual frequency, including zero. The value $\mathrm{sgn}_0(0) = 1$ chooses the positive limiting branch only for the zero bin. In contrast to an absolute-value replacement, (39) preserves reflections caused by negative components of u for a nonsymmetric window and therefore agrees with the signed D_u in (11). This is a numerical convention, not an extension of a continuous theorem to a singular scale.

For one u and one orientation, direct evaluation at all b costs $O(N^2)$ operations, whereas Equation (38) costs $O(N\log N)$ [17]. For N_u analyzed frequencies, the respective costs are $O(N_uN^2)$ and $O(N_uN\log N)$. The CLCST adds one input chirp and one output phase multiplication to the CST, both $O(N)$ per applicable array; hence both transforms and a consistently implemented left-sided version have the same leading complexity. If a nonradial window is swept over N_θ orientations, the cost becomes $O(N_\theta N_u N\log N)$ and full storage becomes $O(N_\theta N_u N)$; streaming over (u,θ) retains $O(N)$ working memory.

Equivalently, if the grid is described by its side length n so that $N = n^2$, the per-frequency FFT cost is $O(n^2\log n)$; the two notations describe the same scaling.

Discrete reconstruction follows Theorem 1: sum $S_u[b]e^{I\gamma\|b\|^2}\Delta x$ over b, apply the inverse FFT with the stated normalization, and right-multiply by $e^{-I\gamma\|x\|^2}$.

4.3. Concentration and Error Measures

For a candidate γ, let $S_{\gamma,j}[b,k]$ denote the jth complex-array coefficient of the discrete CLCST, where $j \in \{0,1\}$ corresponds to the representation (34). The collapsed arrays and their total coefficient energy are

$$G_{\gamma,j}[k] = \Delta x\sum_b S_{\gamma,j}[b,k]e^{\mathrm{i}\gamma\|b\|^2}, \qquad E_\gamma[k] = |G_{\gamma,0}[k]|^2 + |G_{\gamma,1}[k]|^2.$$

Thus, with the sum over k taken across the complete discrete frequency grid, define

$$p_\gamma[k] = \frac{E_\gamma[k]}{\sum_\ell E_\gamma[\ell]}, \quad H_2(\gamma) = -\log\sum_k p_\gamma[k]^2, \quad C_{\mathrm{peak}}(\gamma) = \max_k p_\gamma[k]. \tag{40}$$

The first quantity is the order-two Rényi entropy and the second is normalized peak concentration [18,19]. Lower H_2 and higher C_{peak} indicate stronger frequency concentration. Chirp estimation uses

$$\widehat{\gamma} = \arg\min_{\gamma\in\Gamma} H_2(\gamma). \tag{41}$$

This criterion is tied directly to the CLCST collapse identity rather than to a qualitative surface plot.

For the two-component resolution experiment, let $P_\gamma(u_1) = \sum_{u_2} E_\gamma(u_1, u_2)$. If P_L and P_R are the maxima on the negative and positive frequency half-axes and P_V is the minimum between their locations, define the operational valley-depth score

$$R_{\text{valley}}(\gamma) = 1 - \frac{P_V}{\min\{P_L, P_R\}}. \tag{42}$$

We call two components resolved when $R_{\text{valley}} \geq 0.1$. This threshold is stated explicitly as a reproducible comparison rule; it is not claimed to be a universal Rayleigh criterion.

For validation, all relative errors use the coefficient norm induced by (4). Additive Clifford noise is scaled to the prescribed ratio $20\log_{10}(\|f\|_2/\|n\|_2)$.

5. Numerical Experiments

All experiments were rerun in MATLAB R2025b with random seed 20260914. Unless otherwise stated, the spatial domain is $[-4, 4)^2$ and the unit-integral Gaussian window is

$$\psi_\sigma(y) = \frac{1}{2\pi\sigma^2} \exp\left(-\frac{\|y\|^2}{2\sigma^2}\right), \qquad \sigma = 0.82, \tag{43}$$

with its discrete samples renormalized to unit integral. Radiality makes the window exactly independent of $R_{-\theta}$, so $\theta = 0$ is fixed rather than estimated in these experiments. Before the task-level comparisons, the defining sum, reversed-kernel FFT algorithm, factorization, and full-grid reconstruction were evaluated on four-component Clifford fields with distinct shifted Gaussian envelopes and phases. Table 1 shows agreement at double-precision roundoff. All six figures were exported at 600 dpi; the accompanying source and CSV files contain every plotted and tabulated value. The MATLAB implementation, complete numerical outputs, saved experiment workspace, and exact Hubble image input used for these experiments are provided in Supplementary File S1.

Table 1. Numerical verification of the right-sided, reversed-kernel fast Fourier transform (FFT) implementation. Errors are relative coefficient-norm errors.

$N_1 = N_2$	Direct–FFT Error	Factorization Error	Reconstruction Error
24	4.06×10^{-16}	4.06×10^{-16}	9.44×10^{-16}
32	1.68×10^{-16}	1.68×10^{-16}	8.60×10^{-16}
48	9.14×10^{-16}	9.14×10^{-16}	1.75×10^{-15}

The even Gaussian makes $\kappa^\vee = \kappa$ and is therefore unable to detect a correlation/convolution sign error. We separately use the nonsymmetric unit-integral window

$$\psi_{\text{ns}}(y) = \frac{1}{2\pi\sigma^2} \exp\left[-\frac{\|y - (0.55, -0.35)\|^2}{2\sigma^2}\right] \tag{44}$$

on a 32×32 grid at $u = (-2\delta, 3\delta)$, where $\delta = 2\pi/8$. Table 2 compares the defining sum with the corrected FFT and with the two discarded shortcuts. The corrected error remains at roundoff, whereas both shortcuts change the coefficients by more than 50%. This test isolates the kernel direction and frequency-sign conventions that the Gaussian experiments would otherwise conceal.

Table 2. Nonsymmetric-window stress test. Each entry is a relative coefficient-norm difference from the defining sum.

Reversed-Kernel FFT	Unreversed-Kernel Shortcut	Unsigned-Scale Shortcut
8.04×10^{-16}	5.26×10^{-1}	5.14×10^{-1}

Together, Tables 1 and 2 confirm that the implementation follows the analyzed right-sided transform. The following experiments evaluate concentration, robustness, multicomponent behavior, phase correction, frequency resolution, and computational cost.

5.1. Chirp Matching and Comparison with the CST

Consider the scalar-plus-bivector-compatible test signal

$$f_\kappa(x) = \exp\left[-\frac{(x_1+0.35)^2}{2(0.72)^2} - \frac{(x_2-0.25)^2}{2(0.95)^2}\right] e^{-I\kappa\|x\|^2}, \qquad \kappa = 1.4, \tag{45}$$

sampled on a 32×32 grid. We scan $\Gamma = \{-3, -2.8, \ldots, 3\}$. Figure 3 shows a unique entropy minimum at the true chirp rate. Table 3 compares the CST ($\gamma = 0$) with the matched CLCST.

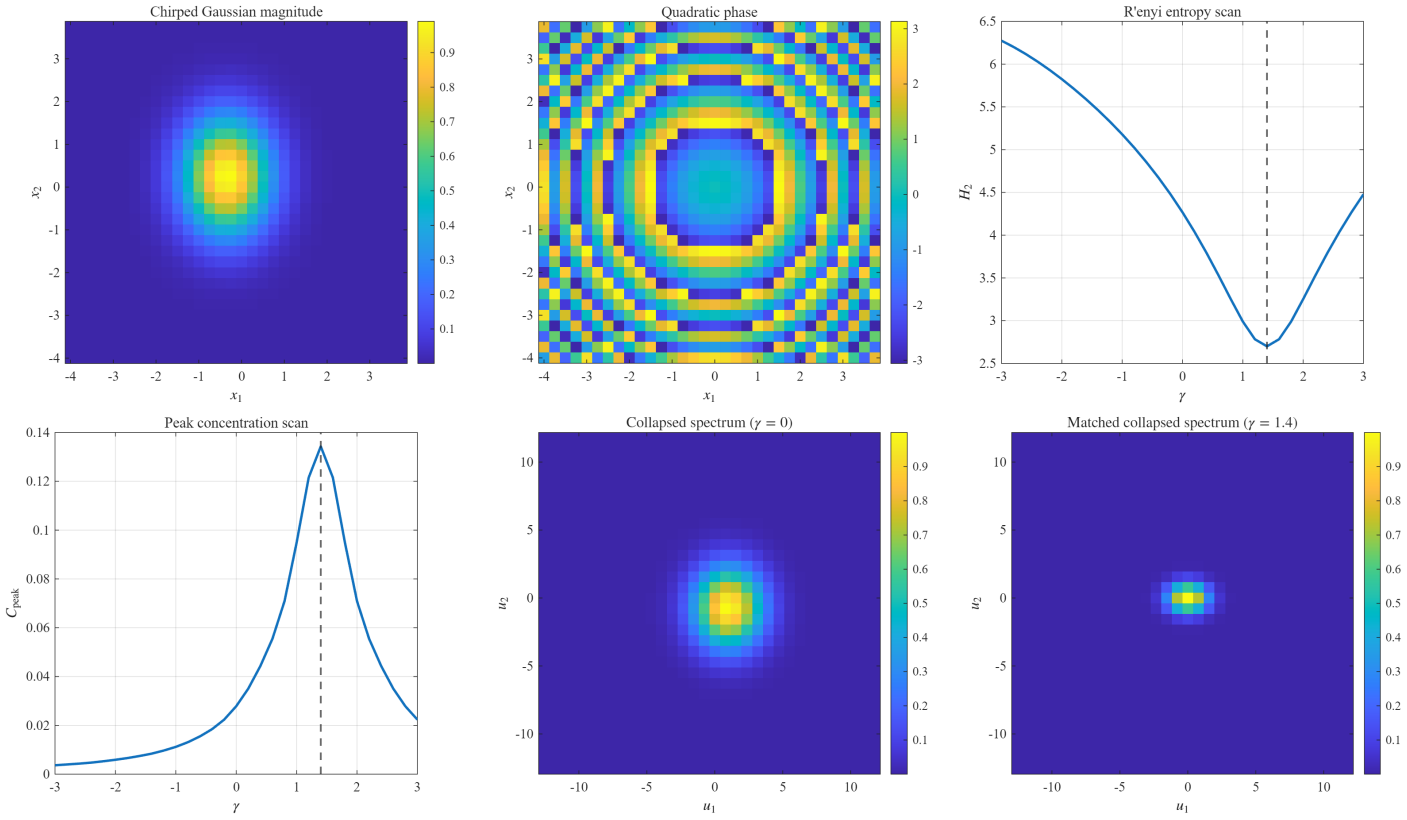

Figure 3. Chirp matching for a two-dimensional Gaussian envelope: signal magnitude and phase, entropy and peak-concentration scans, and collapsed spectra for the CST and the matched CLCST.

Table 3. Quantitative CST–CLCST comparison for the Gaussian chirp.

κ	$\widehat{\gamma}$	$\lvert\widehat{\gamma} - \kappa\rvert$	$H_2(0)$	$H_2(\widehat{\gamma})$	$C_{\text{peak}}(0)$	$C_{\text{peak}}(\widehat{\gamma})$
1.4	1.4	0	4.2674	2.7006	0.02783	0.13429

Matching reduces the entropy by 36.7% and increases peak concentration by a factor of 4.82. This is not a claim that every CLCST parameter is superior to the CST: the gain

occurs when the scanned chirp ratio matches quadratic phase, precisely as predicted by Corollary 1.

5.2. Noise Robustness

Independent scalar–bivector Gaussian noise is added at several signal-to-noise ratios (SNRs). Ten trials are used at each finite SNR, and the same entropy grid is scanned. Figure 4 and Table 4 report the estimates. The clean case is listed once.

The true grid point is recovered in every trial from 20 through 0 dB for this fixed-seed experiment. At -5 dB the mean absolute error is 0.06, but at -10 dB it rises to 0.30 with a standard deviation of 0.37, exceeding one scan increment. The low-SNR result therefore documents degradation and does not support a claim of uniformly stable recovery.

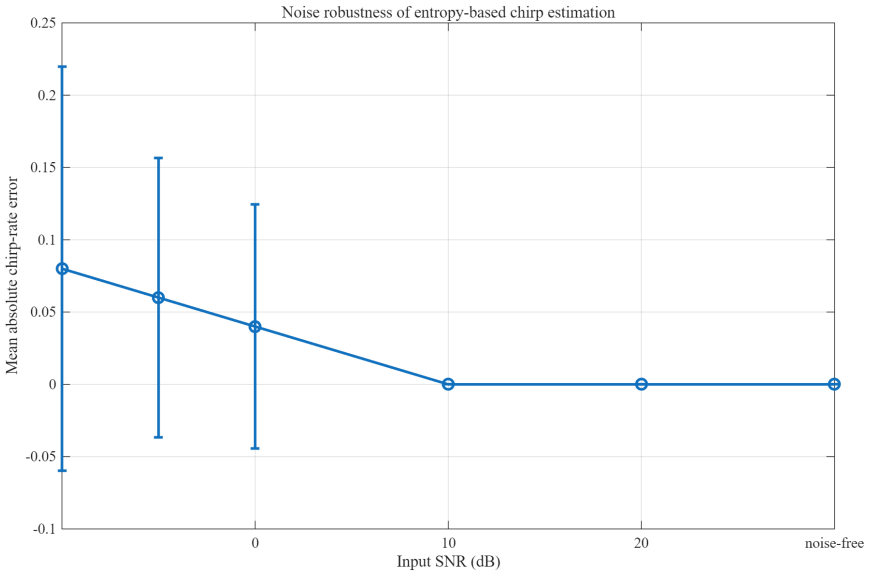

Figure 4. Noise robustness of entropy-based chirp-rate estimation. Points show individual trials; error bars summarize the finite-SNR trials.

Table 4. Noise robustness over the fixed scan grid. Values are the mean ± standard deviation.

SNR (dB)	Estimated γ	Absolute Error
∞	1.400	0.000
20	1.400 ± 0.000	0.000 ± 0.000
10	1.400 ± 0.000	0.000 ± 0.000
0	1.400 ± 0.000	0.000 ± 0.000
-5	1.380 ± 0.114	0.060 ± 0.097
-10	1.500 ± 0.474	0.300 ± 0.368

5.3. A Genuine Four-Component Clifford Signal

To exercise the algebra rather than repeat a scalar example, we form

$$f = f_0 + f_1 e_1 + f_2 e_2 + f_{12} I, \tag{46}$$

where the four spatially shifted Gaussian components have chirp rates $-1.8, -0.6, 0.8$, and 1.8, respectively. The components are encoded jointly through (34). Figure 5 shows the component envelopes and their controlled ground-truth entropy scans. Table 5 also reports a joint-transform linearity check.

Table 5. Chirp-rate recovery for the four Clifford basis components.

Component	True κ	Estimated γ	Absolute Error	Joint Linearity Residual
f_0	-1.8	-1.8	2.22×10^{-16}	3.48×10^{-16}
f_1	-0.6	-0.6	1.11×10^{-16}	3.48×10^{-16}
f_2	0.8	0.8	2.22×10^{-16}	3.48×10^{-16}
f_{12}	1.8	1.8	2.22×10^{-16}	3.48×10^{-16}

Because each ground-truth rate lies on the scan grid, the noise-free recovery error is numerical roundoff. The more relevant Clifford check is that the transform of the joint field agrees with the sum of the four embedded component transforms to 3.48×10^{-16}. This confirms the fixed right-action convention used in both the theory and code.

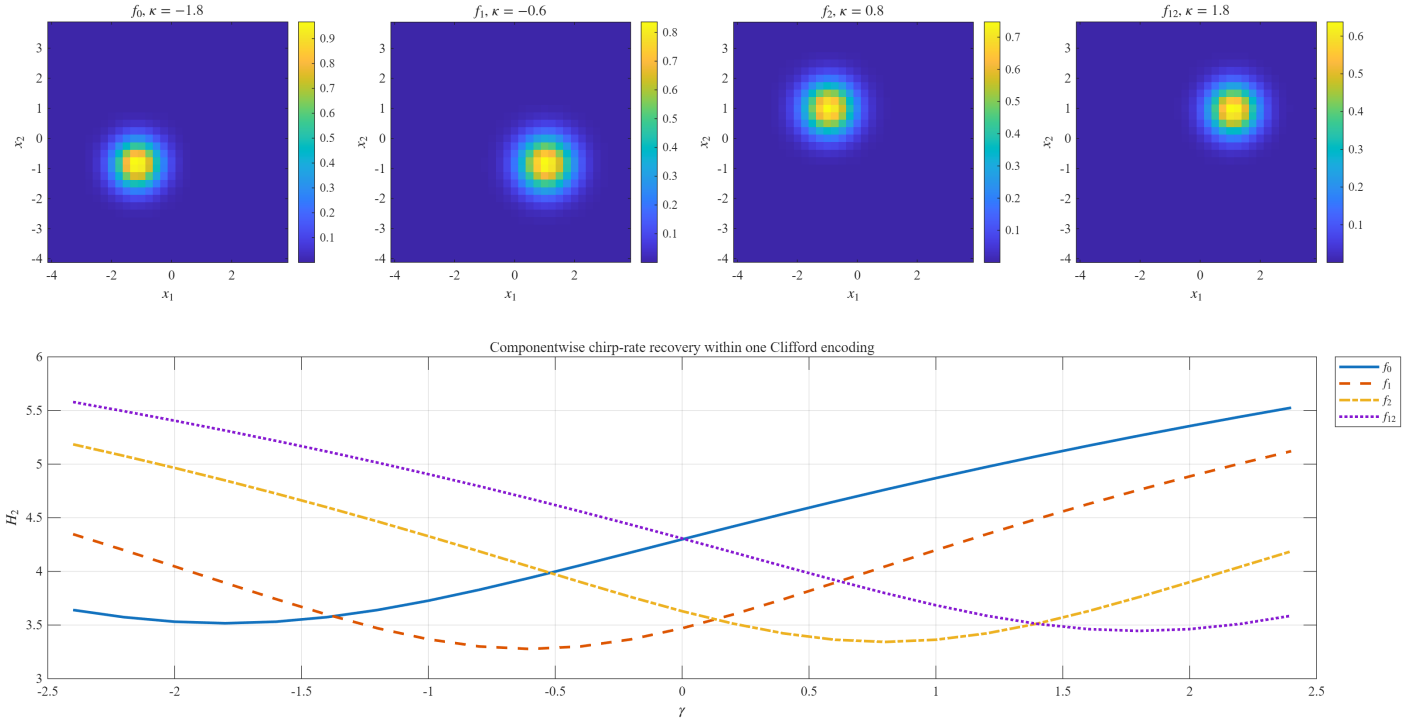

Figure 5. Four-component $\mathrm{Cl}_{0,2}$ signal. (**Top**): coefficient-field envelopes and assigned chirp rates. (**Bottom**): componentwise entropy curves computed with the same Clifford implementation.

5.4. Noisy Modified Shepp–Logan Imaging Benchmark

The next imaging experiment uses the modified Shepp–Logan phantom, a standard benchmark in computational imaging derived from an analytically specified ellipse model [20]. The 48×48 image is multiplied by $e^{-I\|x\|^2}$ and corrupted by complex Clifford noise at 5 dB. The purpose is to model a known quadratic phase error, as occurs in Fourier imaging, and test whether the proposed parameter restores spectral concentration. Table 6 reports the quantitative comparison, and Figure 6 shows the input, transformed spectra, and entropy scan.

Table 6. CST–CLCST comparison for the noisy imaging benchmark.

κ	$\widehat{\gamma}$	$\lvert\widehat{\gamma} - \kappa\rvert$	$H_2(0)$	$H_2(\widehat{\gamma})$	$C_{\mathrm{peak}}(0)$	$C_{\mathrm{peak}}(\widehat{\gamma})$
1.0	1.0	0	6.2381	3.8947	0.01210	0.12287

The matched transform lowers entropy by 37.6% and increases peak concentration by a factor of 10.15 despite the 5 dB noise. The benchmark therefore tests a computationally meaningful phase-compensation task rather than only visualizing a transform kernel.

5.5. Measured Hubble Image with Controlled Phase Aberration

To move beyond analytically generated data, we use the 1995 NASA/ESA Hubble Space Telescope WFPC2 observation of NGC 6543 (the Cat's Eye Nebula), documented by NASA [21]. We retain rows 1–560 and columns 21–580 of the downloaded RGB image to remove its documentary margins, sample 64 uniformly spaced indices in each direction, and normalize each channel by its maximum. The resulting 64×64 channels are embedded as

$$f_{\text{obs}} = R + Ge_1 + Be_2, \tag{47}$$

or, equivalently, $(z_0, z_1) = (R, G - \mathrm{i}B)$ in (34). Thus, all three measured channels are processed jointly as one $\mathrm{Cl}_{0,2}$ field.

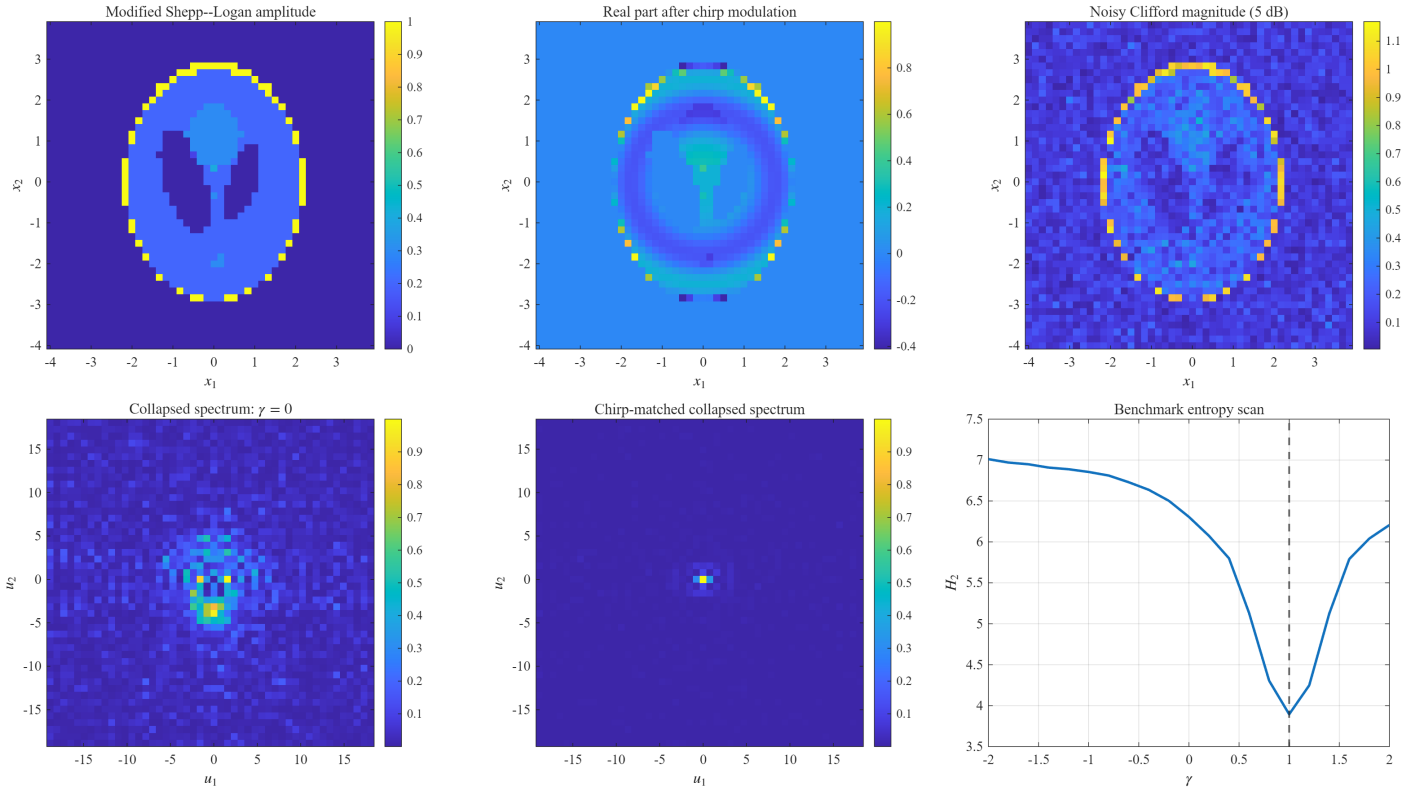

Figure 6. Modified Shepp–Logan benchmark with quadratic phase and 5 dB noise: amplitude, chirped real part, noisy magnitude, CST and chirp-matched collapsed spectra, and the entropy scan.

The image itself does not include a calibrated wavefront-error map. We therefore impose the known Fourier-imaging aberration $e^{-I\kappa\|x\|^2}$ with $\kappa = 0.8$ and then estimate it from the aberrated observation. This is a controlled real-data experiment: the spatial content is measured, while the phase error is injected to provide a ground truth. Because right multiplication by a unit chirp preserves the coefficient norm, magnitude-only images would conceal the correction. The first and last panels of Figure 7 therefore render the phase-sensitive scalar, e_1, and e_2 coefficient channels as RGB, while Table 7 supplies the invariant quantitative comparison.

Table 7. CST–CLCST comparison on the measured Hubble image with controlled phase aberration.

κ	$\widehat{\gamma}$	$H_2(0)$	$H_2(\widehat{\gamma})$	$C_{\text{peak}}(0)$	$C_{\text{peak}}(\widehat{\gamma})$	Residual at $\gamma = 0$	Matched Residual
0.8	0.8	4.1973	2.2595	0.04699	0.24475	1.4036	1.06×10^{-16}

The estimate recovers the imposed phase coefficient exactly on the 0.1 scan grid. Relative to the CST value $\gamma = 0$, entropy falls by 46.2% and peak concentration increases by a factor of 5.21. These values are not universal performance constants: they are the descriptive ratios for this cropped, resampled image and injected $\kappa = 0.8$. Their mechanism is exact, however. Equation (28) shows that the CST summary contains the Fourier spectrum of the still-aberrated field, whereas the matched summary contains the spectrum of its dechirped measured envelope. Right multiplication by the estimated inverse chirp consequently reduces the relative Clifford reconstruction residual from 1.4036 to numerical roundoff.

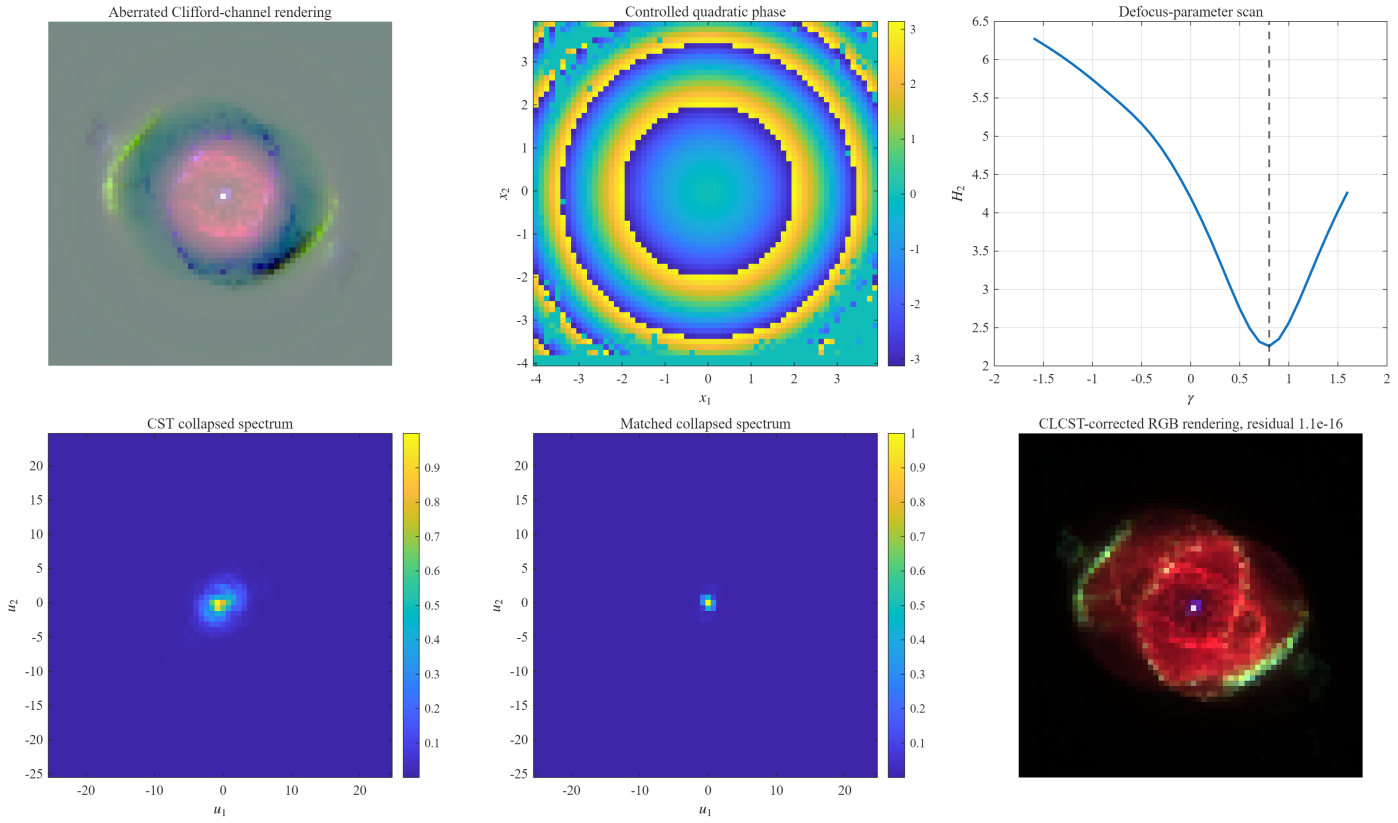

Figure 7. Measured Hubble NGC 6543 observation with controlled quadratic phase: phase-sensitive aberrated coefficient-channel rendering, imposed phase, entropy scan, CST and matched collapsed spectra, and the CLCST-corrected RGB rendering. Image credit: NASA/ESA, J.P. Harrington and K.J. Borkowski.

5.6. Frequency Resolution and Measured Computational Speedup

We next analyze two equal-energy Gaussian-envelope components centered at frequencies $\pm\Delta/2$ and carrying the common chirp rate $\kappa = 1$. The CST and the matched CLCST use the same samples and concentration calculation; only γ changes. Table 8 reports (42). The CST produces a single broadened feature for every tested separation. Under the stated 0.1 valley rule, the matched CLCST resolves the pair at every tested $\Delta \geq 2.0$ and does not resolve it at $\Delta \leq 1.5$ on the 64×64 grid. The frequency-bin spacing is $2\pi/8 \approx 0.785$, so these observations bracket the operational transition in $1.5 < \Delta_{\text{crit}} \leq 2.0$ (approximately 1.91–2.55 bins); they do not identify an exact or universal resolution limit. The transition reflects the dechirped Gaussian spectral width, sampling, and the chosen valley threshold.

Table 8. Two-component frequency-resolution comparison. A score of at least 0.1 is classified as resolved.

Δ	CST Score	Matched Score	CST Resolved	Matched Resolved
3.5	0	0.993	No	Yes
3.0	0	0.967	No	Yes
2.5	0	0.819	No	Yes
2.0	0	0.491	No	Yes
1.5	0	0	No	No
1.0	0	0	No	No

Finally, the defining correlation sum and the equivalent reversed-kernel convolution (38) are timed on a 32×32 grid while producing all translations for the same frequency set. Figure 8 juxtaposes the operational resolution score with the measured direct-to-FFT speedup, and Table 9 reports the wall-clock values. The FFT code is approximately 159–164 times faster in this run, while Tables 1 and 2 establish agreement with the defining sum at roundoff. These measurements compare implementations of the same CLCST; they do not claim that the CLCST is asymptotically cheaper than either the CST or its quaternion-equivalent realization.

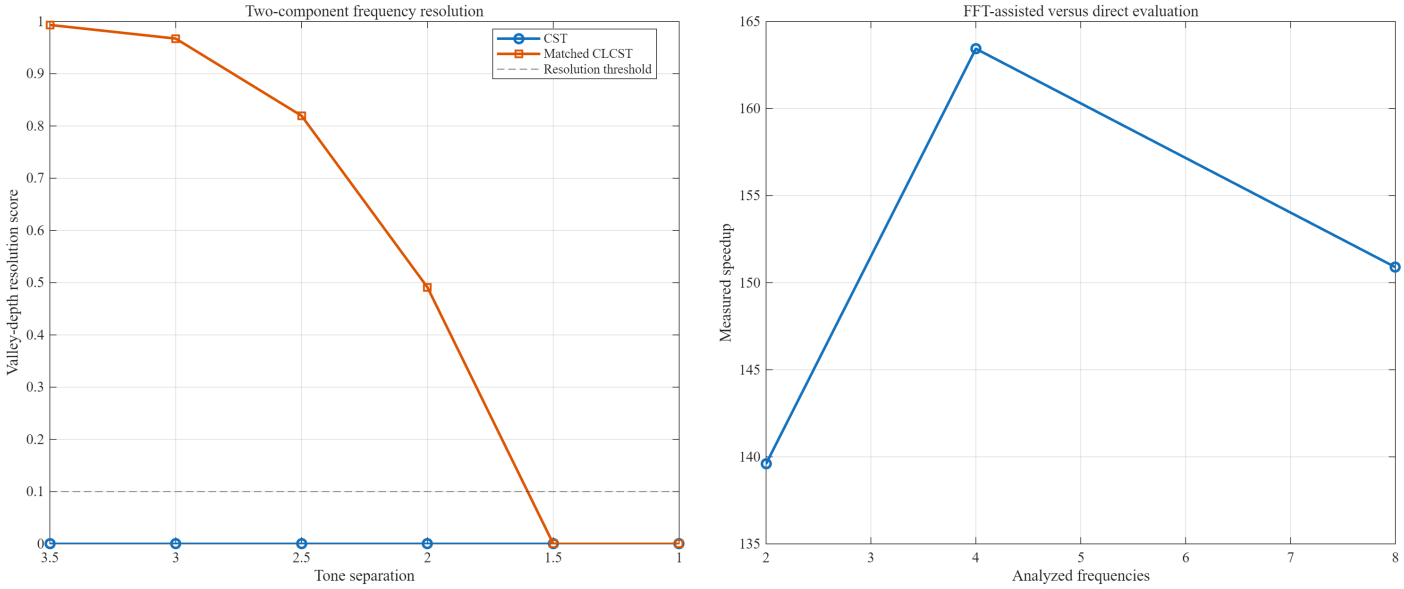

Figure 8. (**Left**): operational frequency-resolution score for the CST and matched CLCST. (**Right**): measured direct-to-FFT speedup when all translations are evaluated.

Table 9. Measured runtime of direct and FFT-assisted CLCST evaluation on a 32×32 grid.

Analyzed Frequencies	Direct (s)	FFT-Assisted (s)	Speedup
2	0.0624	0.000380	164.1
4	0.1031	0.000636	162.1
8	0.2028	0.001275	159.1

6. Discussion

6.1. Scope and Relation to Quaternion Formulations

The present algebra is not more general than the quaternions: $\mathrm{Cl}_{0,2} \cong \mathbb{H}$ and both have four real degrees of freedom. Existing quaternionic Stockwell and Q-LCST theories therefore provide the closest benchmarks [11,12]. The existing Q-LCST uses a two-sided quaternion kernel, whereas the present transform fixes all oscillatory factors on the right and uses a real scalar window. These are different operator conventions, so their identities cannot be combined by moving phases through quaternion-valued quantities. The benefit

established here is correspondingly specific: an order-safe factorization links the right-sided CLCT, CST, dechirping, and direct reconstruction, and the implementation tests exactly that factorization. There is no claimed intrinsic accuracy or complexity advantage over a consistently defined right-sided quaternion algorithm; under the isomorphism, such an algorithm is the same computation.

6.2. Interpretation of Concentration and Resolution

The concentration gains follow from an exact cancellation rather than from an extra number of algebraic channels. For $f_\kappa = ae^{-I\kappa\|x\|^2}$, choosing $\gamma = \kappa$ makes $C_\gamma f_\kappa = a$; hence the collapsed CLCST energy is the Fourier energy of the unchirped envelope, while the CST retains the dispersive phase. This explains the entropy and peak-concentration improvements. Their numerical sizes—including the Hubble reductions of 46.2% and the factor 5.21—depend on the signal, injected phase, grid, scan, and metric. They are empirical effect sizes, not bounds guaranteed by the theory.

The two-tone study similarly supports only an operational statement. On the stated grid and with the stated valley criterion, the threshold lies between the two tested separations 1.5 and 2.0. Increasing the spatial aperture refines the Fourier grid, whereas changing the envelope width or threshold changes the valley depth. This explains why the reported result should not be extrapolated as a continuous-resolution constant.

6.3. Window and Orientation Tradeoffs

The Gaussian is smooth, localized, positive, and has unit integral, so it supports Theorem 1 and retains the low-frequency component. Its lack of vanishing moments, however, makes it less selective against slowly varying backgrounds. A derivative-of-Gaussian (DOG) window has zero mean and can suppress such backgrounds or emphasize edges and bands, but then $\int \psi = 0$: the inner b-integral in (27) vanishes, and the present direct inversion cannot be used. A DOG-based analyzer would need a separately derived dual-window/frame reconstruction or an added low-pass channel. This is a design tradeoff rather than a free substitution.

The rotation parameter disappears from the experiments only because the Gaussian in (43) is radial. For an anisotropic or nonsymmetric window, θ controls orientation and must be reported or estimated. A sweep over N_θ orientations multiplies both the time and full-storage costs by N_θ, as stated in Section 4; streaming avoids the full-storage factor but not the computation.

6.4. Multiplication Side, Higher Dimensions, and Local Chirps

A left-sided formulation does not lose the two-complex-array advantage. As shown in Section 4, it acts as $(z_0, z_1) \mapsto (e^{it}z_0, e^{-it}z_1)$ and therefore uses two complex FFTs with an opposite sign in the second channel. Its leading cost is the same, but all covariance, CLCT-relation, and reconstruction formulas must be rederived with the new order.

Higher-dimensional Clifford algebras are not obtained by changing a subscript. In $\mathrm{Cl}_{0,3}$ the pseudoscalar $e_1e_2e_3$ squares to $+1$, so it cannot replace the present imaginary unit. A possible route is to select a fixed element J satisfying $J^2 = -1$ and seek a compatible complex-array decomposition for FFT implementation. However, the precise decomposition, computational complexity, positivity, covariance, norm behavior, and rotational interpretation depend on the algebra and the selected J and require a separate derivation. We therefore make no higher-dimensional algorithmic or theoretical claim in the present work.

Finally, a single γ compensates one global isotropic quadratic phase. Scanning N_γ candidates multiplies the analysis cost by N_γ (and by N_θ if orientations are also swept). Locally varying or anisotropic chirps require tiled estimation, ridge tracking, or a matrix-

valued local phase model. Those modifications sacrifice the present single global collapse-and-invert formula unless a compatible synthesis theory is developed.

7. Conclusions

We have formulated the right-sided $Cl_{0,2}$-valued CLCST with explicit multiplication order and with its quaternion equivalence stated. Standard Clifford conjugation gives a positive real Hilbert norm, real scalar windows remove hidden reordering, and the canonical dependence is stated explicitly through $\gamma = A/(2B)$. The corrected CLCT relation keeps its output phase on the right. The exact chirp–CST–dechirp factorization explains why matching a quadratic phase converts a dispersed component into its unchirped envelope. The transform also admits direct inversion for unit-integral windows and a reversed-kernel FFT implementation with the same leading complexity as the CST and its one-sided quaternion equivalent.

Quantitative experiments verify the defining identities at machine precision, and a nonsymmetric-window test separately validates the kernel direction and signed frequency scale. The examples demonstrate improved concentration, operationally bracketed component resolution, pronounced acceleration over direct evaluation, joint processing of a four-component field, and controlled phase correction on measured Hubble content. The limitations are equally explicit: the method addresses a global quadratic phase in $Cl_{0,2}$, the reported effect sizes are signal-specific, a DOG window needs a different synthesis theory, orientation and chirp sweeps multiply cost, and higher-dimensional Clifford extensions require new proofs. Within this stated scope, the method is a rigorously defined chirp-adaptive extension of the right-sided CST.

Supplementary Materials: The following supporting information can be downloaded at https://www.mdpi.com/article/10.3390/mca31050203/s1: the MATLAB source file `generate_mca_revision_experiments.m`; CSV files containing the numerical values reported in the verification and experiment tables, including all noise trials; the saved experiment workspace; and the measured Hubble image input used in Section 5.5.

Author Contributions: Conceptualization, Y.-Q.X. and B.-Z.L.; methodology, Y.-Q.X.; software, Y.-Q.X.; validation, Y.-Q.X. and B.-Z.L.; formal analysis, Y.-Q.X.; investigation, Y.-Q.X.; data curation, Y.-Q.X.; writing—original draft preparation, Y.-Q.X.; writing—review and editing, Y.-Q.X. and B.-Z.L.; visualization, Y.-Q.X.; supervision, B.-Z.L.; project administration, B.-Z.L.; funding acquisition, B.-Z.L. All authors have read and agreed to the published version of the manuscript.

Funding: This research was funded by the National Natural Science Foundation of China, grant number 62571042, and the Natural Science Foundation of Beijing Municipality, grant number 4242011.

Data Availability Statement: The MATLAB source, generated CSV tables, experiment workspace, and exact Hubble image input are supplied as reproducibility files with the revised submission. The measured NGC 6543 observation used in Section 5.5 is publicly documented by NASA [21]; the remaining test signals are generated by the supplied source. No new external dataset was created.

Conflicts of Interest: The authors declare no conflicts of interest.

References

1. Stockwell, R.G.; Mansinha, L.; Lowe, R.P. Localization of the complex spectrum: The S transform. *IEEE Trans. Signal Process.* **1996**, *44*, 998–1001. [CrossRef]
2. Stockwell, R.G. A basis for efficient representation of the S-transform. *Digit. Signal Process.* **2007**, *17*, 371–393. [CrossRef]
3. Moukadem, A.; Bouguila, Z.; Abdeslam, D.O.; Dieterlen, A. A new optimized Stockwell transform applied on synthetic and real non-stationary signals. *Digit. Signal Process.* **2015**, *46*, 226–238. [CrossRef]
4. Hutníková, M.; Mišková, A. Continuous Stockwell transform: Coherent states and localization operators. *J. Math. Phys.* **2015**, *56*, 073504. [CrossRef]

5. Riba, L.; Wong, M.W. Continuous inversion formulas for multi-dimensional modified Stockwell transforms. *Integral Transforms Spec. Funct.* **2015**, *26*, 9–19. [CrossRef]
6. Almeida, L.B. The fractional Fourier transform and time-frequency representations. *IEEE Trans. Signal Process.* **1994**, *42*, 3084–3091. [CrossRef]
7. Ozaktas, H.M.; Arikan, O.; Kutay, M.A.; Bozdagi, G. Digital computation of the fractional Fourier transform. *IEEE Trans. Signal Process.* **1996**, *44*, 2141–2150. [CrossRef]
8. Wei, D.Y.; Zhang, Y.J. Fractional Stockwell transform: Theory and applications. *Digit. Signal Process.* **2021**, *115*, 103090. [CrossRef]
9. Wei, D.Y.; Zhang, Y.J.; Li, Y.M. Linear canonical Stockwell transform: Theory and applications. *IEEE Trans. Signal Process.* **2022**, *70*, 1333–1347. [CrossRef]
10. Shah, F.A.; Teali, A.A.; Bahri, M. Clifford-valued Stockwell transform and the associated uncertainty principles. *Adv. Appl. Clifford Algebras* **2022**, *32*, 25. [CrossRef]
11. Akila, L.; Roopkumar, R. Quaternionic Stockwell transform. *Integral Transforms Spec. Funct.* **2016**, *27*, 484–504. [CrossRef]
12. Bhat, M.Y.; Dar, A.H. Quaternion linear canonical S-transform and associated uncertainty principles. *Int. J. Wavelets Multiresolut. Inf. Process.* **2023**, *21*, 2250035. [CrossRef]
13. Pei, S.-C.; Ding, J.-J.; Chang, J.-H. Efficient implementation of quaternion Fourier transform, convolution, and correlation by 2-D complex FFT. *IEEE Trans. Signal Process.* **2001**, *49*, 2783–2797. [CrossRef]
14. Lounesto, P. *Clifford Algebras and Spinors*, 2nd ed.; Cambridge University Press: Cambridge, UK; 2001.
15. Hitzer, E.; Nitta, T.; Kuroe, Y. Applications of Clifford's geometric algebra. *Adv. Appl. Clifford Algebras* **2013**, *23*, 377–404. [CrossRef]
16. Shah, F.A.; Teali, A.A. Clifford-valued linear canonical transform: Convolution and uncertainty principles. *Optik* **2022**, *265*, 169436. [CrossRef]
17. Cooley, J.W.; Tukey, J.W. An algorithm for the machine calculation of complex Fourier series. *Math. Comput.* **1965**, *19*, 297–301. [CrossRef]
18. Rényi, A. On measures of entropy and information. In *Proceedings of the Fourth Berkeley Symposium on Mathematical Statistics and Probability*; University of California Press: Berkeley, CA, USA, 1961; Volume 1, pp. 547–561.
19. Stanković, L. A measure of some time-frequency distributions concentration. *Signal Process.* **2001**, *81*, 621–631. [CrossRef]
20. Shepp, L.A.; Logan, B.F. The Fourier reconstruction of a head section. *IEEE Trans. Nucl. Sci.* **1974**, *21*, 21–43. [CrossRef]
21. NASA Science. Cat's Eye Nebula, NGC 6543. 1995. Available online: https://science.nasa.gov/asset/hubble/cats-eye-nebula/ (accessed on 13 August 2026).

Disclaimer/Publisher's Note: The statements, opinions and data contained in all publications are solely those of the individual author(s) and contributor(s) and not of MDPI and/or the editor(s). MDPI and/or the editor(s) disclaim responsibility for any injury to people or property resulting from any ideas, methods, instructions or products referred to in the content.